catalysts

MDPI

Article

Selectivity Control of CO_2 Reduction over Pt/g-C_3N_4 Photocatalysts under Visible Light

Andrey A. Saraev, Anna Y. Kurenkova, Angelina V. Zhurenok, Evgeny Y. Gerasimov and Ekaterina A. Kozlova *

Federal Research Center, Boreskov Institute of Catalysis SB RAS, Lavrentieva Ave. 5, 630090 Novosibirsk, Russia
* Correspondence: kozlova@catalysis.ru

Abstract: Photocatalysts based on g-C_3N_4 have been investigated in the CO_2 reduction reaction under visible light irradiation (λ = 397, 427, 452 nm). Photocatalysts were prepared by melamine calcination at 500–600 °C with further platinum deposition (0.1–1.0 wt.%). The effect of the preparation conditions of g-C_3N_4 and the method of platinum deposition on the physicochemical properties and activity of photocatalysts was studied. The photocatalysts were investigated by X-ray photoelectron spectroscopy, X-ray absorption spectroscopy, X-ray diffraction, high resolution transmission electron microscopy, UV-Vis spectroscopy, and low temperature nitrogen adsorption techniques. It has been found that the efficiency of CO_2 reduction is governed by the surface area of g-C_3N_4 and the presence of platinum in the metallic state, while the optimal content of platinum is 0.5 wt. %. The highest rate of CO_2 reduction achieved over Pt/g-C_3N_4 photocatalyst is 13.2 μmol h^{-1} g^{-1} (397 nm), which exceeds the activity of pristine g-C_3N_4 by 7 times. The most active photocatalysts was prepared by calcining melamine in air at 600 °C, followed by modification with platinum (0.5 wt.%).

Keywords: photocatalysis; photocatalytic CO_2 reduction; g-C_3N_4; platinum; visible light; CH_4 production

check for updates

Citation: Saraev, A.A.; Kurenkova, A.Y.; Zhurenok, A.V.; Gerasimov, E.Y.; Kozlova, E.A. Selectivity Control of CO_2 Reduction over Pt/g-C_3N_4 Photocatalysts under Visible Light. *Catalysts* **2023**, *13*, 273. https://doi.org/10.3390/catal13020273

Academic Editors: Farid Orudzhev and Irina A. Zvereva

Received: 29 December 2022
Revised: 19 January 2023
Accepted: 21 January 2023
Published: 25 January 2023

1. Introduction

Due to the growing concentration of greenhouse gases in the atmosphere, their utilization attracts a special attention [1,2]. The main component is CO_2, which is produced by burning fossil fuels [3]. Other important issues are the growing energy consumption and the depletion of fossil fuels [4]. Thus, the conversion of CO_2 to synthetic fuels would solve several problems at once. Such an opportunity is provided during the photocatalytic process of CO_2 reduction, the products of which are CH_4, CO, CH_3OH, etc. [5,6]. Moreover, when using sunlight as the radiation source, photocatalytic CO_2 conversion becomes an ideal green technology for solar-to-chemical conversion [7]. However, most of the described photocatalysts have a rather low efficiency when irradiated with visible light, which makes up a large part of the solar spectrum [8,9].

A quantity of compounds is used as photocatalysts, among which TiO_2 has received tremendous attention [10–16]. However, TiO_2-based photocatalysts are predominantly activated by irradiation of ultraviolet light only [17]. Compared to photocatalysts based on metal oxides, g-C_3N_4 has a fairly narrow band gap, which makes it a promising photocatalyst for processes under the visible light irradiation [18–22]. Additionally, a strongly negative conduction band potential (−1.1 V vs. NHE) is favorable for CO_2 reduction [23]. Low cost, simplicity of preparation, and absence of toxicity make g-C_3N_4 an attractive photocatalyst from a practical point of view [24]. However, the photogenerated electrons and holes in a pristine g-C_3N_4 undergo rapid recombination, that leads to a decrease in photocatalytic activity [25]. To enhance the lifetime of charge carriers, metal deposition on the surface of g-C_3N_4 is shown to be one of the most effective techniques [26]. Platinum is

widely used as a cocatalyst due to its high work function of electrons, which greatly improves charge separation [27]. This way, development of a composite material Pt/g-C_3N_4 has a positive effect on photocatalyst efficiency and CO_2 reduction rate.

It is known that the synthesis conditions have a decisive influence on the properties and activity of the photocatalyst [28]. One of the most widely applied methods for synthesis g-C_3N_4 is thermal condensation of low-cost and non-toxic melamine at temperature around 400–600 °C [29,30]. Temperature variation leads to a significant modification in the morphology of the product, and, therefore, to a great extent alter the photocatalytic activity of g-C_3N_4. Additionally, the method of platinum deposition affects the photocatalytic activity. Depending on the synthesis procedure, Pt particles could be distributed differently on the surface. In case of aggregation of metal particles, the photocatalyst will demonstrate poor activity [31]. Thus, the relationship between preparation conditions, photocatalyst morphology, and photocatalytic activity is critical for determining approaches to the synthesis of highly active materials.

In the current work, we have shown the effect of preparation conditions on the morphology of g-C_3N_4 particles and the state of platinum, and, therefore, reveal the key factors that determine the activity of photocatalysts based on g-C_3N_4 in the photocatalytic reduction of CO_2. The possibility of controlling the selectivity for CO_2 reduction over Pt/g-C_3N_4 photocatalysts by changing the wavelength of the light source has been shown for the first time.

2. Results and Discussion

In this work, a series of g-C_3N_4-based photocatalyst modified with Pt particles was prepared. On the first stage, calcination temperature of melamine was varied in a range of 500–600 °C. After that, the Pt particles were deposited on the surface of g-C_3N_4 by two methods: the photochemical reduction or photodeposition method (PD) and by reduction with $NaBH_4$ or chemical deposition (CD). The obtained photocatalysts were characterized by different techniques and studied in CO_2 reduction reaction (CO_2 RR) under visible light irradiation. Three LEDs were used as a radiation source: LED-397 (maximum intensity at λ = 397 nm), LED-427 (maximum intensity at λ = 427 nm), and LED-452 (maximum intensity at λ = 452 nm). The obtained photocatalysts were labeled as: X% Pt(PD or CD)/g-C_3N_4 T, where X–mass content of Pt, PD or CD – method of Pt deposition, T – calcination temperature of melamine.

2.1. Photocatalyst Characterization

To study the influence of the synthesis temperature on the textural characteristics of the samples obtained, g-C_3N_4 samples were tested by low temperature nitrogen adsorption method. The raise of synthesis temperature promotes the increase of surface area (Table 1). The growth of the specific surface area at a higher temperature is caused by an increase in the crystallinity of resulting g-C_3N_4. It is known that an increased surface area allows more active components to be deposited and also facilitates light absorption of the catalyst and adsorption of reagents.

Table 1. Properties of synthesized g-C_3N_4 in dependence of calcination temperature of melamine.

T, °C	Specific Surface Area, $m^2\ g^{-1}$	Pore Volume, $cm^3 \cdot g^{-1}$	Band Gap Energy, eV	[N]/[C]
500	9.4	0.06	2.82	1.31
600	26.4	0.14	2.75	1.37

The optical properties of the synthesized g-C_3N_4 samples were studied using UV-Vis spectroscopy (Figure 1a). Absorption edges slightly decrease from 2.82 to 2.75 eV with the increase in calcination temperature (Figure 1b), which corresponds to the band gap of g-C_3N_4 [28,32]. X-ray diffraction pattern (Figure S1) demonstrates a dominant peak at 2θ≈28°, that is attributed to the (002) plane of g-C_3N_4 [33].

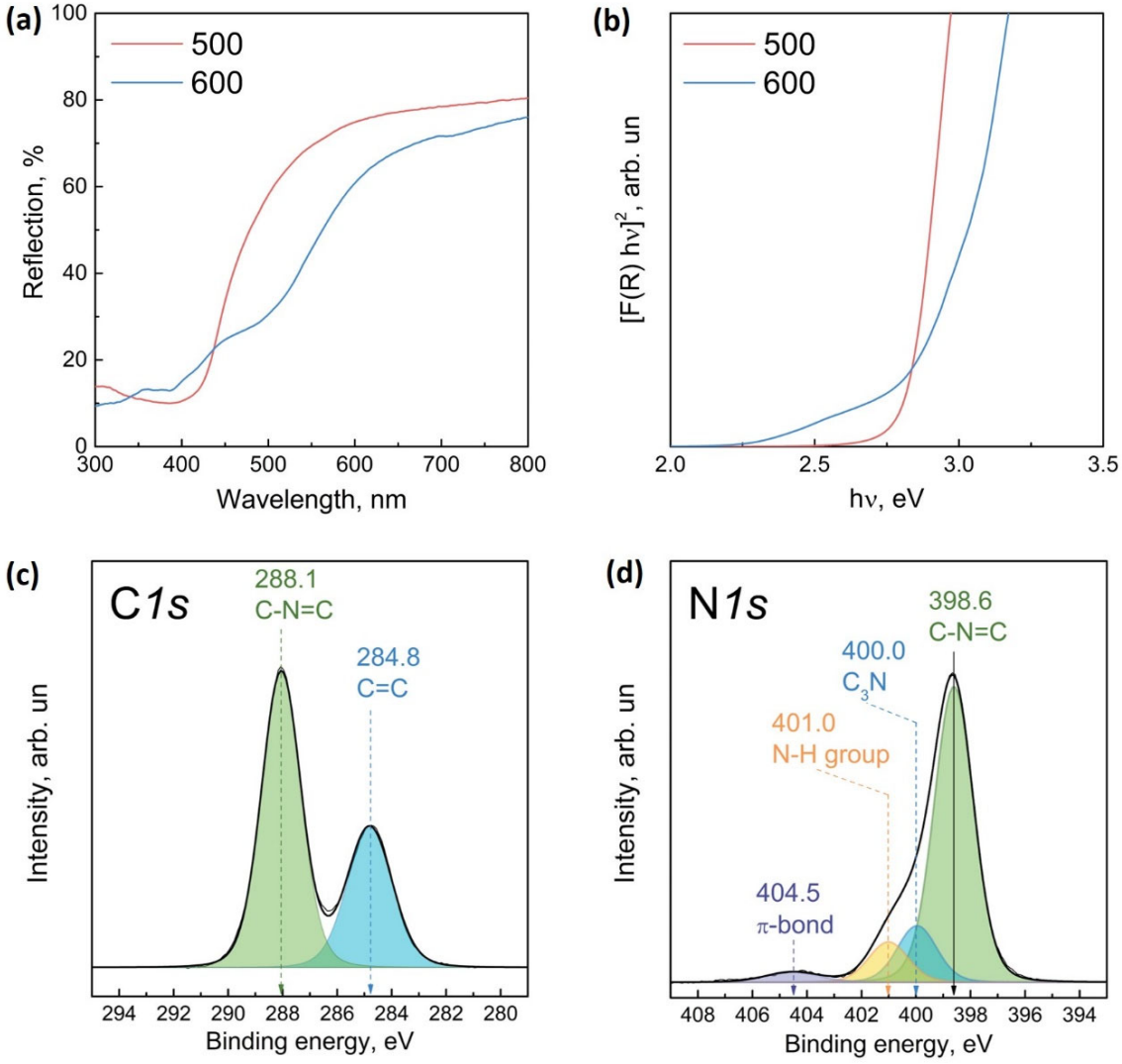

Figure 1. Diffuse reflectance spectra of g-C_3N_4 (**a**) and Tauc's plots depending on the calcination temperature of melamine (**b**); C*1s* (**c**) and N*1s* (**d**) core-level spectra of g-C_3N_4 obtained from melamine at 600 °C. The N*1s* spectrum is normalized to the integral intensity of the C*1s* peak corresponding to the spectrum of g-C_3N_4.

Additionally, the [N]/[C] ratio remains constant in the obtained catalysts. The C*1s* and N*1s* core-level spectra of g-C_3N_4 obtained at 600 °C are shown in Figure 1c,d. The C*1s* spectrum is well described by two peaks with binding energies at 284.8 and 288.1 eV. The first peak corresponds to carbon-containing impurities present on the surface of the photocatalyst under study (often used to calibrate the binding energy scale). The second peak is characteristic of C*1s* g-C_3N_4 and corresponds to carbon forming bonds with nitrogen atoms in the g-C_3N_4 structure [34,35]. In the case of the N*1s* spectrum, four peaks are observed with binding energies at 398.6, 400.0, 401.0, and 404.5 eV. According to the literature, the first peak refers to nitrogen atoms forming a C–N=C bond, the second one—to the N-$(C)_3$ bond with three carbon atoms, and the third one—to the N-H terminal groups [34,35]. The fourth peak corresponds to an excited π-bond.

Therefore, we can conclude the synthesized photocatalysts are g-C_3N_4 with similar properties except surface area.

As mentioned above, two methods of platinum deposition on g-C_3N_4 were used: photodeposition (PD) and chemical reduction (CD). The key characteristics of catalysts affected the catalytic process are the oxidation state, surface concentration, and size distribution of

nanoparticles of active components and could be varied depending on synthesis conditions. To determine these parameters, the catalysts Pt(CD)/g-C_3N_4 600 and Pt(PD)/g-C_3N_4 600 obtained by depositing platinum on g-C_3N_4 synthesized from melamine calcined at 600 °C were investigated by UV-Vis spectroscopy, X-ray photoelectron spectroscopy (XPS), high resolution transmission electron microscopy (HR TEM), and X-ray absorption spectroscopy.

Figure 2 represents the characterization results for platinized photocatalysts. Compared to unmodified samples of g-C_3N_4, the deposition of Pt promotes light absorption in region beyond 450 nm (Figure 2a,b), which is caused by localized surface plasmon resonance of platinum nanoparticles [36]. Broadening the absorption spectrum of photocatalysts favorably affects the rate of a photocatalytic reaction under the visible light irradiation.

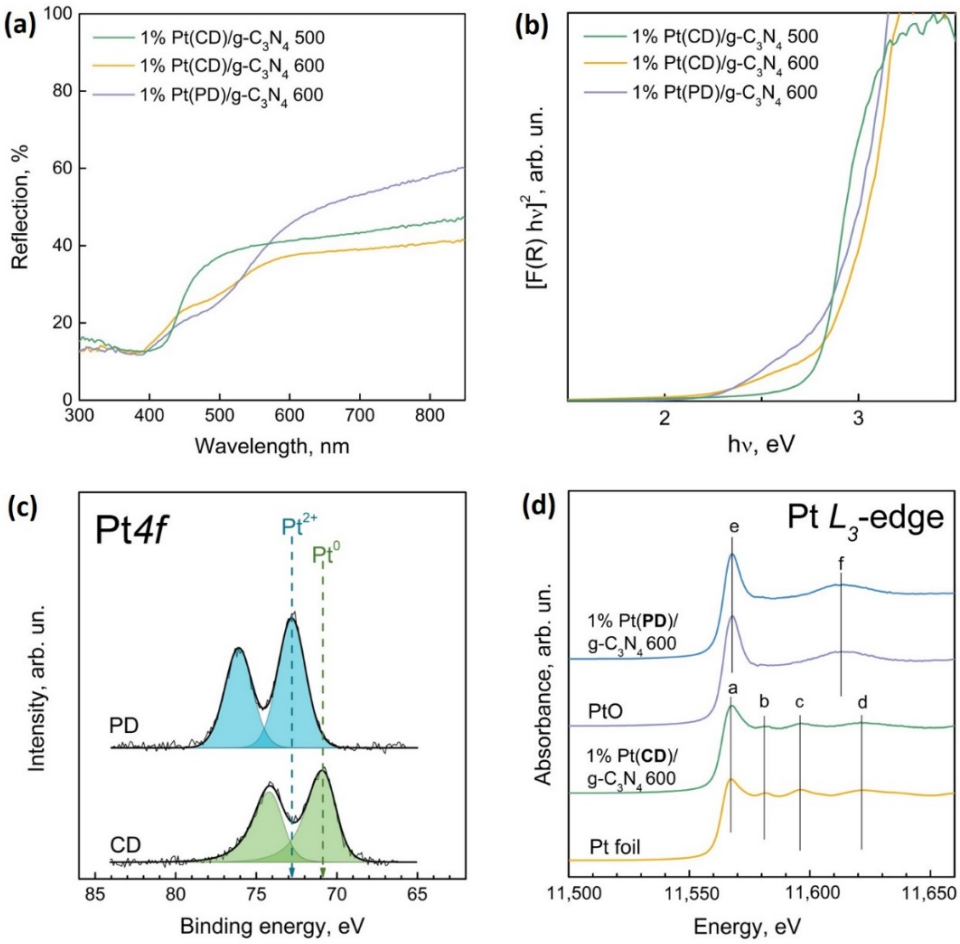

Figure 2. Diffuse reflectance spectra of 1%Pt/g-C_3N_4 (**a**) and Tauc's plots depending on the deposition method of Pt (**b**); Pt*4f* core-level spectra (**c**) and Pt L_3-edge (**d**) spectra of Pt in 1%Pt/g-C_3N_4 catalyst obtained from melamine at 600 °C. The Pt*4f* core-level spectrum is normalized to the integral intensity of the C*1s* core-level peak corresponding to the spectrum of g-C_3N_4.

Figure 2c shows the Pt*4f* core-level spectra of 1% Pt/g-C_3N_4 photocatalyst obtained from melamine at 600 °C. In the case of chemical reduction, the Pt*4f* core-level spectrum is approximated by one Pt$4f_{7/2}$-Pt$4f_{7/2}$ doublet with a Pt$4f_{7/2}$ binding energy at 70.9 eV. When Pt particles were deposited by photoreduction, a Pt$4f_{7/2}$ binding energy is about 72.7 eV. In the literature, for bulk metallic platinum, the Pt$4f_{7/2}$ binding energy is about 71.1–71.6 eV [37,38]. For bulk PtO, PtO_2, and $Pt(OH)_4$, the binding energies of Pt$4f_{7/2}$ lie in the range of 72.3–73 eV, 74.0–74.1 eV, and 74.2–74.4 eV [39–42]. Thus, using chemical reduction deposition method platinum exist in the metallic state, while in the case of the photoreduction method, Pt is in the oxidized state Pt^{2+} in the form of PtO.

The surface atomic ratios of element measured by XPS are presented in Table 2. One can see that the deposition of platinum by chemical reduction leads to formation of metallic platinum nanoparticles. In contrast, the photoreduction of platinum leads to the formation of platinum oxide. Lowering the temperature calcination of melamine leads to an increase in [Pt]/[C] ratio, which is due to the different specific surface of the synthesized g-C_3N_4 samples (Table 2).

Table 2. Relative atomic concentrations of elements in the surface layer of the catalysts, as well as the fraction of platinum in the metallic state.

Photocatalyst	[N]/[C]	[Pt]/[C]	%, Pt^0	[O_x]/[C]
0.5% Pt(CD)/g-C_3N_4 600	1.36	0.002	100	0.17
1% Pt(CD)/g-C_3N_4 500	1.31	0.006	100	0.12
1% Pt(CD)/g-C_3N_4 600	1.39	0.004	100	0.08
0.5% Pt(PD)/g-C_3N_4 600	1.36	0.005	0	0.10
1% Pt(PD)/g-C_3N_4 600	1.43	0.005	0	0.04

X-ray absorption spectroscopy was additionally used to determine the bulk structure of platinum nanoparticles deposited on g-C_3N_4. The X-ray absorption near edge structure (XANES) spectra of the Pt L_3-edge of the 1% Pt/g-C_3N_4 photocatalysts obtained from melamine upon calcination at 600 °C and with different methods of platinum deposition, as well as reference compounds of platinum—metal foil and PtO are shown in Figure 2d. The XANES spectra of the L_3-edges of Pt catalysts have different shapes, which indicates a different phase composition of platinum nanoparticles. Thus, the spectrum of the L_3-edge of the Pt in catalyst 1% Pt(CD)/g-C_3N_4 600 has the same structure as the spectrum of metal platinum (platinum foil). Indeed, the structure of the absorption spectra of 1% Pt(CD)/g-C_3N_4 600 and metallic platinum has a number of common features (peaks a-d), therefore, platinum nanoparticles are completely metallic and do not have a core–shell structure. At the same time, the spectrum of the L_3-edge of the Pt catalyst 1% Pt(PD)/g-C_3N_4 600 has the same structure as the spectrum platinum oxide PtO. The structure of the absorption spectra of 1% Pt(PD)/g-C_3N_4 600 and platinum oxide has a number of common features (peaks e and f), which allows us to state that platinum nanoparticles in this photocatalyst are completely oxidized and also do not have the core–shell structure.

The HR TEM images showed that platinum is uniformly distributed over the g-C_3N_4 surface (Figures 3 and S2). However, in the case of using chemical reduction, aggregates of several platinum nanoparticles are predominantly formed (Figure 3a). When Pt deposited using photoreduction, a larger number of single nanoparticles is observed (Figure 3b). The average size of platinum nanoparticles was about 7 nm and 4 nm for samples synthesized using chemical reduction and photoreduction, respectively.

Thus, applied methods allow us to study the structural and textural characteristics of the synthesized photocatalysts, that makes it possible to reveal the effect of these parameters on the activity and selectivity of photocatalysts in the photocatalytic CO_2 RR.

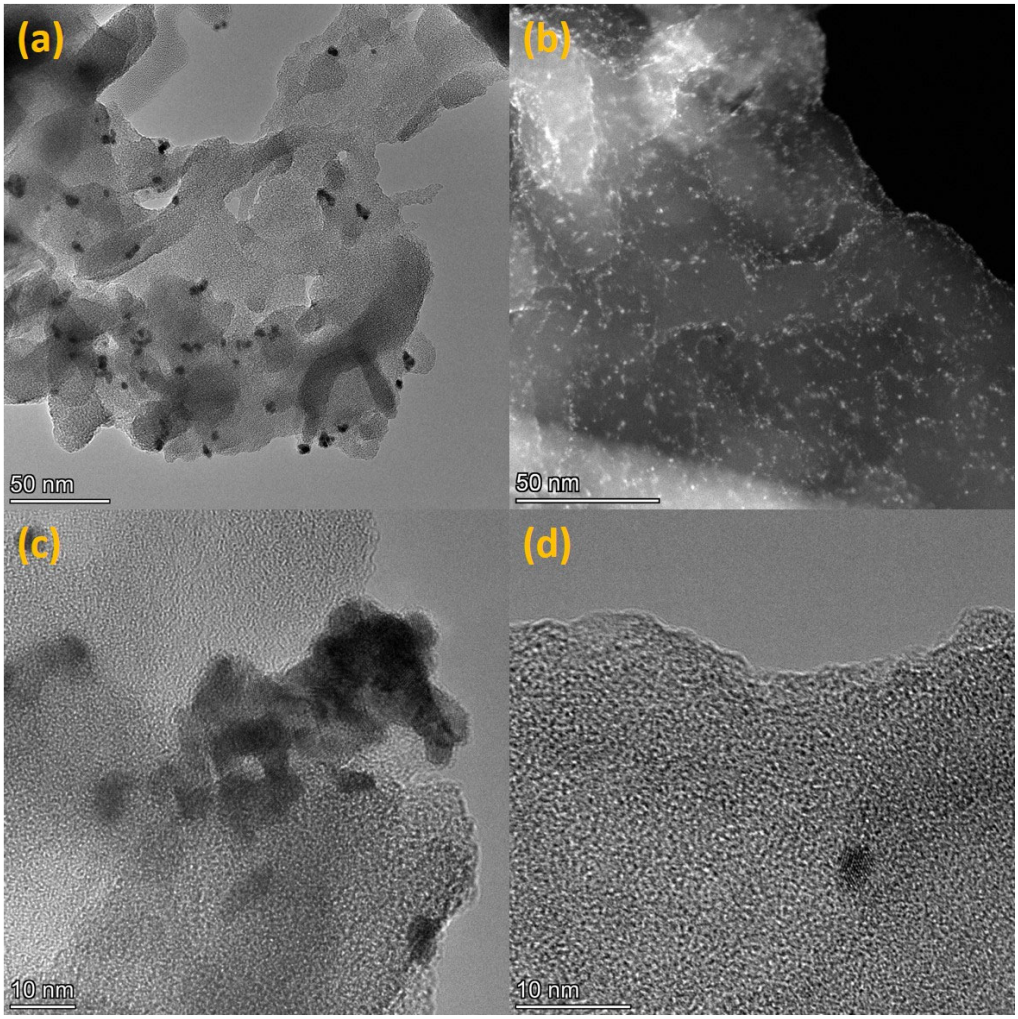

Figure 3. HR TEM images of 0.5% Pt(CD)/g-C_3N_4 600 (**a**,**c**), HAADF STEM (**b**), and HR TEM (**d**) images of 0.5% Pt(PD)/g-C_3N_4 600.

2.2. Photocatalytic Activity

The activity of the synthesized photocatalysts was studied in the reaction of CO_2 reduction under the irradiation of LED-397, LED-427, and LED-452 with the addition of 1 mL of water in the reactor. At the first stage, the influence of the melamine calcination temperature on the activity of the obtained photocatalysts 1% Pt/g-C_3N_4 was studied. The highest rates of CH_4 formation and overall CO_2 reduction rate are achieved over the samples obtained at 600 °C (Figure 4), which is explained by the largest specific surface of the samples (Table 1) and, as a result, a high number of adsorption sites.

A study of the activity of photocatalysts showed that the deposition of platinum (0.5 and 1 wt.%) leads to a significant increase in the rate of CH_4 formation, while the rate of CO formation changes insignificantly (Figure 5a,b). Thus, by varying the content of platinum, it is possible to increase or decrease the selectivity of methane formation. Variation of the deposition method and platinum content showed that chemical reduction is more effective—the formation of metallic Pt is beneficial for methane formation and overall CO_2 reduction (Figure 5c).

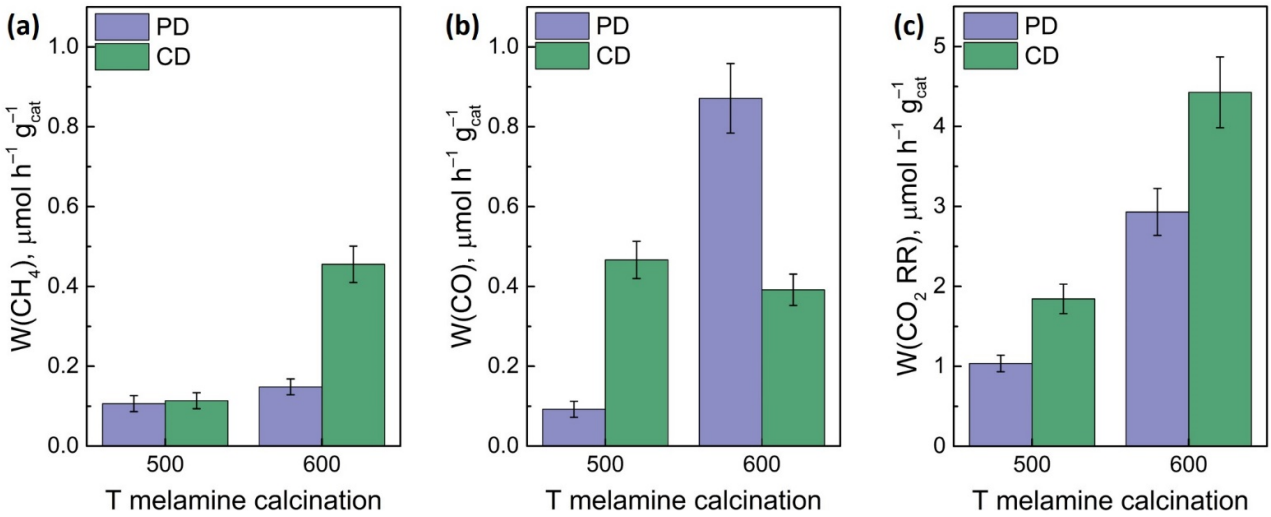

Figure 4. The formation rate of CH_4 (**a**), CO (**b**), and overall CO_2 reduction rate (**c**) in dependence on melamine calcination temperature and platinum deposition technique. Photocatalysts: 1% Pt/g-C_3N_4 500, 1% Pt/g-C_3N_4 600. Conditions: m(cat.) = 30 mg, $P_0(CO_2)$ = 1 atm, t(reaction) = 24 h, λ = 397 nm.

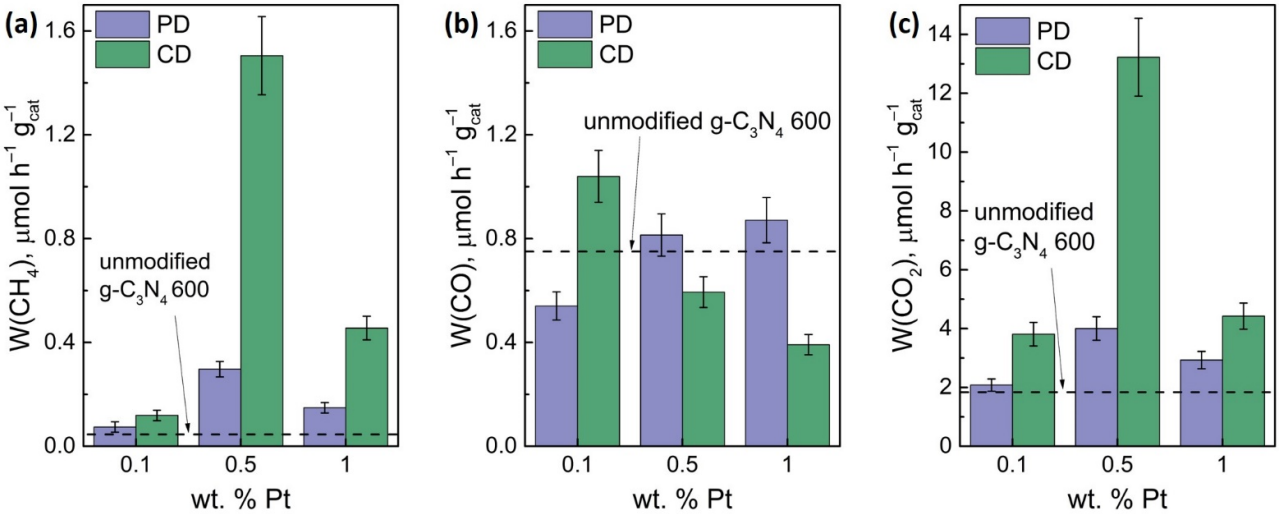

Figure 5. The formation rate of CH_4 (**a**), CO (**b**), and overall CO_2 reduction rate (**c**) in dependence on platinum concentration and platinum deposition technique. Photocatalysts: (0.1–1)% Pt/g-C_3N_4 600. Conditions: m(cat.) = 30 mg, $P_0(CO_2)$ = 1 atm, t(reaction) = 24 h, λ = 397 nm.

The highest rate of total reduction of CO_2 was achieved over the 0.5% Pt(CD)/g-C_3N_4 600 photocatalyst and equal to 13.2 μmol h^{-1} g^{-1} under irradiation with λ = 397 nm, which exceeds the activity of unmodified g-C_3N_4 obtained by calcining melamine at 600 °C by a factor of 7.

The most active photocatalysts 0.5% Pt(CD)/g-C_3N_4 600 and 0.5% Pt(PD)/g-C_3N_4 600 were tested in the CO_2 RR using LED-427 and LED-452 as sources of light irradiation (Figure 6). The highest activity was demonstrated by the sample obtained from melamine at 600 °C and modified with platinum by the chemical deposition method (0.5% Pt(CD)/g-C_3N_4 600). Under LED-427 irradiation, the overall CO_2 reduction rate was 6.2 μmol h^{-1} g^{-1} (AQE = 0.13%).

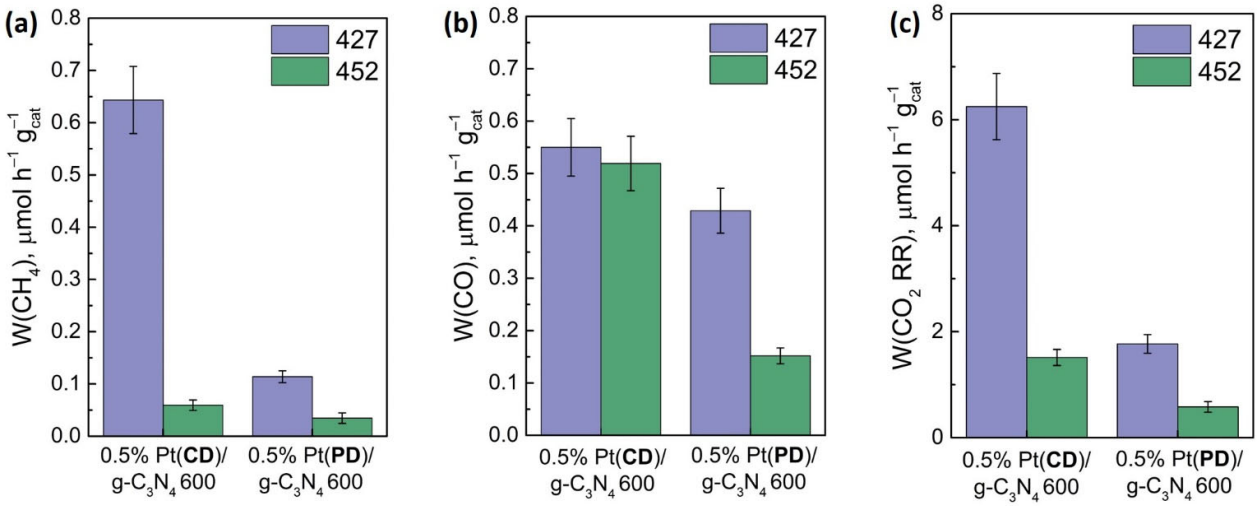

Figure 6. The formation rate of CH_4 (**a**), CO (**b**), and overall CO_2 reduction rate (**c**). Conditions: m(cat.) = 30 mg, $P_0(CO_2)$ = 1 atm, t(reaction) = 24 h, λ = 427 nm or 452 nm.

It should be noted in the presence of water vapor in the reactor, in addition to the photocatalytic CO_2 reduction process (Equations (1) and (2)), a competing reaction of photocatalytic hydrogen formation occurs simultaneously (Equation (3)) [43,44]:

$$CO_2 + 2e^- + 2H^+ = CO + H_2O,\ E^0 = -0.53\ \text{V vs. NHE at pH 7} \quad (1)$$

$$CO_2 + 8e^- + 8H^+ = CH_4 + 2H_2O,\ E^0 = -0.24\ \text{V vs. NHE at pH 7} \quad (2)$$

$$2H_2O + 2e^- = H_2 + 2OH^-,\ E^0 = -0.41\ \text{V vs. NHE at pH 7} \quad (3)$$

Since there are two competitive photocatalytic processes, we have evaluated the selectivity for CO_2 reduction on an electron basis (Table 3).

Table 3. Activity and selectivity of most active Pt/g-C_3N_4.

Photocatalyst	Light Source, nm	Formation Rate, μmol h^{-1} $g_{cat}{}^{-1}$			W (CO_2 RR), μmol h^{-1} $g_{cat}{}^{-1}$	S (CO_2 RR), %
		CO	CH_4	H_2		
0.5% Pt(CD)/ g-C_3N_4 600	397	0.6	1.5	3.7	13.2	51.5
	427	0.6	0.6	0.7	6.2	80.1
	452	0.5	0.1	0.1	1.5	94.8
0.5% Pt(PD)/ g-C_3N_4 600	397	0.8	0.3	1.3	4.0	73.3
	427	0.4	0.1	0.3	1.8	85.6
	452	0.2	0.03	0.1	0.6	87.2

A lower selectivity of 0.5% Pt(CD)/g-C_3N_4 600 compared to 0.5% Pt(PD)/g-C_3N_4 600 is likely to be caused by presence of Pt in metallic state. On the surface of metallic Pt, H_2 can release throw Tafel (Equation (4)) or Heyrovsky mechanism (Equation (5)) [45,46]:

$$2H^{\cdot} = H_2, \quad (4)$$

$$H^{\cdot} + e^- + H^+ = H_2 \quad (5)$$

Thus, metallic platinum promotes both processes—CO_2 reduction and H_2 evolution. Moreover, the rate of CH_4 formation is significantly increased compared to CO when using catalysts with platinum under LED-397 (Figure 5a). Despite the fact that the reduction of CO_2 to CH_4 is a thermodynamically favorable process, it requires $8e^-/8H^+$

to proceed, which causes kinetic difficulties. When deposited on the surface of a semiconductor, platinum acts as an electron trap due to the formation of Schottky barrier at the metal/semiconductor contacts. Metallic Pt has one of the highest work functions of electron 5.65 eV, which allows efficient capture of electrons [27,47]. Thereby, the enrichment of electron density in Pt particles promotes the multielectron process of CH_4 formation.

In the case of PtO/g-C_3N_4 photocatalysts obtained by platinum photodeposition (0.5% Pt(PD)/g-C_3N_4 600), charge separation is less efficient due to the lower electron work function of PtO compared to metallic Pt. Therefore, the total rate of CO_2 reduction is lower than that for the photocatalyst 0.5% Pt(CD)/g-C_3N_4 600. In this case, a higher selectivity of CO_2 reduction is achieved, because PtO particles are likely not suitable cocatalysts for the formation of H_2 from water. Additionally, one can see (Table 3) that for all wavelengths, the rate of CO formation is higher than the rate of CH_4 production.

It should be noted that the selectivity is also the key parameter of photocatalytic process as well as the activity of photocatalyst. As can be seen in Table 3, the decrease in energy of a photon with an increase in wavelength inhibits the H_2 formation rate in a greater extent than the overall CO_2 reduction reaction. A similar effect was previously shown for Ni_3Mn-layered double hydroxide photocatalyst [48]. Due to a lower Gibbs free energy barrier for CO_2 activation than for H_2 evolution, H_2 formation is suppressed when irradiated with low photon energy light. The processes of photocatalytic reduction of CO_2 and H_2 evolution on Pt/g-C_3N_4 photocatalysts likely have similar features.

Thus, by changing the wavelength of the light source, it is possible to control the selectivity of the photocatalytic reduction of carbon dioxide. Despite the activity of photocatalysts not reaching the highest values presented in the literature, even selectivity of 0.5% Pt(CD)/g-C_3N_4 600 photocatalysts under LED-397 exceeds some values described in the literature for CO_2 reduction over semiconductor-based photocatalysts, modified with Pt particles (Table 4).

Table 4. Selectivity and activity of some semiconductor-based photocatalysts presented in the literature.

Photocatalyst	Light Source	Formation Rate, μmol h^{-1} $g_{cat}{}^{-1}$		W (CO_2 RR), μmol h^{-1} $g_{cat}{}^{-1}$	S (CO_2 RR), %	Article
		CO	CH_4			
0.5% Pt-TiO_2	Xe lamp, 400–780 nm (580 mW cm^{-2}), 320–400 nm (60 mW cm^{-2})	1.1	5.2	43.8	40	[49]
3% MgO–0.5% Pt-TiO_2		0.02	6.3	50.4	83	
0.9% Pt-TiO_2	320–780 nm	2.2	11	92.4	41	[50]
1.7% Cu–0.9%Pt-TiO_2		8.3	33	280.6	85	
ZnO/g-C_3N_4	Xe lamp, λ > 420 nm	16.8	30.5	277.6	86	[51]
Bi_2O_3/g-C_3N_4	Xe lamp	2.81	1.34	16.3	86	[52]

Thereby, Pt/g-C_3N_4 photocatalysts prepared with a simple two-step synthesis method demonstrate the high selectivity in the CO_2 reduction reaction.

3. Materials and Methods

3.1. Photocatalyst Synthesis

Synthesis of g-C_3N_4 was carried out from melamine by calcination at different temperature. A ceramic crucible with 2 g of melamine (Sigma-Aldrich, St. Louis, USA, 99%), covered with a lid, was placed in a muffle furnace (Smolenskoye SKTB SPU, Smolensk, Russia) and kept at a certain temperature (500, 600 °C) in air for 2 h. The heating rate to the set temperature was 10 degrees per minute. The resulting sample of g-C_3N_4 was ground in a mortar.

After that, platinum was deposited on g-C_3N_4 surface in two ways: by chemical reduction (CD) and by photodeposition (PD).

In the first case, platinum was deposited on a g-C_3N_4 sample according to the following procedure: a sample of g-C_3N_4 (500 mg) was dispersed using ultrasound, impregnated with an 0.02 M H_2PtCl_6 (Reakhim, Moscow, Russia, 98%) solution, followed by reduction with an excess of $NaBH_4$ (Acros Organics, Geel, Belgium, 99%) solution. The resulting photocatalyst was washed in a centrifuge and dried in air at 50 °C for 5 h.

In the second case, a suspension was prepared consisting of a sample of g-C_3N_4 (500 mg) and 40 mL of a 20% solution of ethanol in water and placed into a photocatalytic reactor. The mixture was purged with argon for 30 min and then illuminated with a 380 nm LED (30 V, 1 A) for 3 h. The resulting photocatalyst was washed in a centrifuge and dried in air at 50 °C for 5 h.

The amount of deposited platinum on g-C_3N_4 was 0.1, 0.5, and 1 wt. %.

3.2. Photocatalyst Characterization

The photocatalysts were characterized by UV-Vis optical absorption spectroscopy, X-ray photoelectron spectroscopy (XPS), X-ray absorption spectroscopy, high-resolution transmission electron microscopy (HR TEM), including the high-angle annular dark-field scanning transmission electron microscopy (HAADF-STEM) technique, N_2 low-temperature adsorption.

The chemical composition of the catalyst surface was studied by XPS with a photoelectron spectrometer (SPECS Surface Nano Analysis GmbH, Berlin, Germany) using non-monochromatized Al Kα radiation (hυ = 1486.6 eV). The spectrometer was equipped with a PHOIBOS-150 hemispherical analyzer (SPECS Surface Nano Analysis GmbH, Berlin, Germany) and an XR-50 X-ray source with a double Al/Mg anode.

The chemical state of platinum in the bulk of the catalysts was studied using X-ray absorption spectroscopy at the station of the Kurchatov Synchrotron Radiation Source (Moscow, Russia). The electron energy in the storage ring was 2.5 GeV at a beam current of 50–150 mA. To monochromatize synchrotron radiation, we used a silicon single crystal with (111) orientation in the form of a cut-out monoblock mounted on a goniometric head. The energy resolution achieved was $\Delta E/E = 2 \times 10^{-4}$. The X-ray absorption spectra of the catalysts were obtained in transmission geometry. The X-ray beam intensity before and after passing through the sample was measured using ionization chambers equipped with Keithley 6487 digital picoammeters (Keithley Instruments, Ohio, USA).

The microstructure of the photocatalysts was studied by HR TEM using a ThemisZ electron microscope (Thermo Fisher Scientific, Waltham, MA, USA) at an accelerating voltage of 200 kV. The microscope was equipped with a SuperX energy-dispersive spectrometer and a spherical aberration corrector. The maximum resolution of the microscope was 0.06 nm. For the HR TEM analysis, the samples were ultrasonically dispersed onto perforated carbon substrates attached to aluminum grids.

The diffuse reflectance UV-Vis spectra were measured using a UV-2501 PC spectrophotometer with an ISR-240A diffuse reflectance unit (Shimadzu, Kyoto, Japan).

The specific surface area was calculated by the Brunauer-Emmett-Teller method using nitrogen adsorption isotherms measured at liquid nitrogen temperatures with an automatic Micromeritics ASAP 2400 sorptometer (Micromeritics, Norcross, USA).

X-ray diffraction pattern was recorded on a D8 Advance diffractometer equipped with a Lynxeye linear detector (Bruker AXS GmbH, Karlsruhe, Germany). The diffraction patterns were obtained in the 2θ range from 10 to 80° with a step of 0.05° using Cu Kα radiation (λ = 1.5418 Å).

3.3. Photocatalytic Activity Test

The activity of photocatalysts was tested in CO_2 reduction reaction in a batch reactor (170 mL). A photocatalyst (30 mg) was deposited on a glass support and placed in the reactor. After that, the reactor containing 1 mL of water was purged with CO_2 for 1 h, and

the light source was turned on. Details are described elsewhere [31]. In this work, 3 light emitting diodes (LEDs) were used as light sources (Figure 7): LED-397 with maximum intensity at 397 nm (power density 60 mWcm^{-2}), LED-427 with maximum intensity at 427 nm (power density 56 mWcm^{-2}), and LED-452 with maximum intensity at 452 nm (power density 42 mWcm^{-2}).

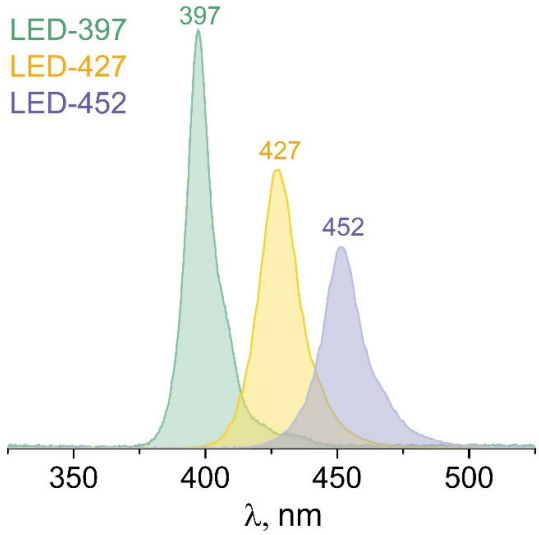

Figure 7. Spectra of LEDs with the wavelength at maximum intensity.

Gas probe was analyzed with a gas chromatograph "GH-1000" (Chromos, Moscow, Russia) equipped with the flame ionization detector and thermal conductivity detector to identify the products of CO_2 reduction and H_2, respectively. The overall rate of CO_2 reduction was calculated according to the following equation:

$$W(\mathrm{CO_2\ RR}) = \frac{8 \times n(\mathrm{CH_4}) + 2 \times n(\mathrm{CO})}{t \times m} \tag{6}$$

where $n(\mathrm{CH_4})$ and $n(\mathrm{CO})$ are the amounts of CH_4 and CO (μmol), 2 and 8 are the coefficients for electron balance, t is the time of reaction (h), and m is the weight of photocatalyst (g).

The selectivity of CO_2 reduction was defined as:

$$S(\mathrm{CO_2RR}) = \frac{8 \times W(\mathrm{CH_4}) + 2 \times W(\mathrm{CO})}{8 \times W(\mathrm{CH_4}) + 2 \times W(\mathrm{CO}) + 2 \times W(\mathrm{H_2})} \times 100\% \tag{7}$$

The apparent quantum efficiency (AQE) was calculated according to the following equation:

$$\mathrm{AQE} = \frac{W(\mathrm{CO_2RR})}{N_{phot}} \times 100\%, \tag{8}$$

where N_{phot} is the calculated photon flux equal to 5.8 mmol h^{-1} for LED-427.

4. Conclusions

In this work, the synthesis conditions were studied for the photocatalytic activity and selectivity of photocatalysts based on g-C_3N_4 modified with Pt or PtO particles. It is shown that the determining factors for reaction efficiency are the surface area of g-C_3N_4 and the oxidation state of the metal. Platinum in the metallic state contributes to an increase in the activity of the photocatalyst, but high selectivity is achieved only at a wavelength of 427 nm and higher. Platinum oxide is a more selective cocatalyst with respect to the photocatalytic reduction of CO_2, but the reaction rate in this case is low. The highest rate of CO_2 reduction achieved over 0.5% Pt(CD)/g-C_3N_4 600 photocatalyst is 13.2 μmol h^{-1} g^{-1} (λ = 397 nm) with selectivity for CO_2 reduction equal to 51.5%. The maximum selectivity is 94.8% and

achieved over the same 0.5% Pt(CD)/g-C_3N_4 600 photocatalyst under irradiation with a wavelength of 450 nm.

Supplementary Materials: The following supporting information can be downloaded at: https://www.mdpi.com/article/10.3390/catal13020273/s1, Figure S1: XRD patterns of the g-C_3N_4 600; Figure S2: HR TEM image of 1% Pt(CD)/g-C_3N_4 600 (a) and HAADF STEM image of 1% Pt(PD)/g-C_3N_4 600 (b).

Author Contributions: Investigation, data curation, visualization, writing—original draft preparation, funding acquisition, project administration, A.A.S.; investigation, data curation, visualization, writing—original draft preparation, A.Y.K.; investigation, data curation, A.V.Z.; investigation, data curation, E.Y.G.; writing—review and editing, supervision, conceptualization, project administration, E.A.K. All authors have read and agreed to the published version of the manuscript.

Funding: This study was supported by Russian Science Foundation (Grant #21-73-10235).

Data Availability Statement: The data presented in this study are available on request from the corresponding author.

Acknowledgments: The XPS and HR TEM experiments were performed using the facilities of the shared research center "National Center of Investigation of Catalysts" at Boreskov Institute of Catalysis. The authors thank Alexander Trigub for the support during the beamtime at the Kurchatov Synchrotron Radiation Source (Kurchatov Institute, Moscow, Russia) and Svetlana Cherepanova for XRD study (Boreskov Institute of Catalysis SB RAS, Novosibirsk, Russia).

Conflicts of Interest: The authors declare no conflict of interest.

References

1. Centi, G.; Perathoner, S. The chemical engineering aspects of CO_2 capture, combined with its utilisation. *Curr. Opin. Chem. Eng.* **2023**, *39*, 100879. [CrossRef]
2. Sreedhar, A.; Ta, Q.T.H.; Noh, J.S. Advancements in the photocatalytic activity of various bismuth-based semiconductor/Ti_3C_2 MXene interfaces for sustainable environmental management: A review. *J. Ind. Eng. Chem.* **2022**, *115*, 26–47. [CrossRef]
3. Hanifa, M.; Agarwal, R.; Sharma, U.; Thapliyal, P.C.; Singh, L.P. A review on CO_2 capture and sequestration in the construction industry: Emerging approaches and commercialised technologies. *J. CO_2 Util.* **2023**, *67*, 102292. [CrossRef]
4. Kouser, S.; Hezam, A.; Ara Khanum, S. Final Rational Design and Engineering of Efficient Metal Organic Framework for Visible Light-driven Photocatalytic carbon-di-oxide Reduction. *Inorg. Chim. Acta* **2022**, *546*, 121287. [CrossRef]
5. Ghosh, U.; Majumdar, A.; Pal, A. Photocatalytic CO_2 reduction over g-C_3N_4 based heterostructures: Recent progress and prospects. *J. Environ. Chem. Eng.* **2021**, *9*, 104631. [CrossRef]
6. Francis Kurisingal, J.; Kim, H.; Hyeak Choe, J.; Seop Hong, C. Covalent organic framework-based catalysts for efficient CO_2 utilization reactions. *Coord. Chem. Rev.* **2022**, *473*, 214835. [CrossRef]
7. Zhao, G.Q.; Long, X.; Zou, J.; Hu, J.; Jiao, F.P. Design of hollow nanostructured photocatalysts for clean energy production. *Coord. Chem. Rev.* **2023**, *477*, 214953. [CrossRef]
8. Tahir, M.B.; Asiri, A.M.; Nawaz, T. A perspective on the fabrication of heterogeneous photocatalysts for enhanced hydrogen production. *Int. J. Hydrogen Energy* **2020**, *45*, 24544–24557. [CrossRef]
9. Chen, S.; Takata, T.; Domen, K. Particulate photocatalysts for overall water splitting. *Nat. Rev. Mater.* **2017**, *2*, 17050. [CrossRef]
10. Yamauchi, M.; Saito, H.; Sugimoto, T.; Mori, S.; Saito, S. Sustainable organic synthesis promoted on titanium dioxide using coordinated water and renewable energies/resources. *Coord. Chem. Rev.* **2022**, *472*, 214773. [CrossRef]
11. Orudzhev, F.F.; Gasanova, F.G.; Aliev, Z.M.; Isaev, A.B. Photoelectrocatalytic oxidation of phenol on platinum-modified TiO_2 nanotubes. *Nanotechnol. Russ.* **2012**, *7*, 482–485. [CrossRef]
12. Kumaravel, V.; Mathew, S.; Bartlett, J.; Pillai, S.C. Photocatalytic hydrogen production using metal doped TiO_2: A review of recent advances. *Appl. Catal. B Environ.* **2019**, *244*, 1021–1064. [CrossRef]
13. Christoforidis, K.C.; Fornasiero, P. Photocatalysis for Hydrogen Production and CO_2 Reduction: The Case of Copper-Catalysts. *ChemCatChem* **2019**, *11*, 368–382. [CrossRef]
14. Ibrahim, I.; Belessiotis, G.V.; Elseman, A.M.; Mohamed, M.M.; Ren, Y.; Salama, T.M.; Mohamed, M.B.I. Magnetic TiO_2/$CoFe_2O_4$ Photocatalysts for Degradation of Organic Dyes and Pharmaceuticals without Oxidants. *Nanomaterials* **2022**, *12*, 3290. [CrossRef]
15. Belessiotis, G.V.; Falara, P.P.; Ibrahim, I.; Kontos, A.G. Magnetic Metal Oxide-Based Photocatalysts with Integrated Silver for Water Treatment. *Materials* **2022**, *15*, 4629. [CrossRef]
16. Kozlova, E.A.; Lyulyukin, M.N.; Markovskaya, D.V.; Selishchev, D.S.; Cherepanova, S.V.; Kozlov, D.V. Synthesis of Cd1-: XZnxS photocatalysts for gas-phase CO_2 reduction under visible light. *Photochem. Photobiol. Sci.* **2019**, *18*, 871–877. [CrossRef]
17. Cheng, S.P.; Wei, L.W.; Wang, H.P. Photocatalytic reduction of CO_2 to methanol by Cu_2O/TiO_2 heterojunctions. *Sustainability* **2022**, *14*, 374. [CrossRef]

18. Fajrina, N.; Tahir, M. A critical review in strategies to improve photocatalytic water splitting towards hydrogen production. *Int. J. Hydrogen Energy* **2019**, *44*, 540–577. [CrossRef]
19. Pan, Z.; Zhao, M.; Zhuzhang, H.; Zhang, G.; Anpo, M.; Wang, X. Gradient Zn-doped poly heptazine imides integrated with a van der Waals homojunction boosting visible light-driven water oxidation activities. *ACS Catal.* **2021**, *11*, 13463–13471. [CrossRef]
20. Zheng, D.; Zhou, J.; Fang, Z.; Heil, T.; Savateev, A.; Zhang, Y.; Antonietti, M.; Zhang, G.; Wang, X. H_2 and CH_4 production from bio-alcohols using condensed poly(heptazine imide) with visible light. *J. Mater. Chem. A* **2021**, *9*, 27370–27379. [CrossRef]
21. Ibrahim, I.; Belessiotis, G.V.; Antoniadou, M.; Kaltzoglou, A.; Sakellis, E.; Katsaros, F.; Sygellou, L.; Arfanis, M.K.; Salama, T.M.; Falaras, P. Silver decorated TiO_2/g-C_3N_4 bifunctional nanocomposites for photocatalytic elimination of water pollutants under UV and artificial solar light. *Results Eng.* **2022**, *14*, 100470. [CrossRef]
22. Zhang, J.; Liang, X.; Zhang, C.; Lin, L.; Xing, W.; Yu, Z.; Zhang, G.; Wang, X. Improved Charge Separation in Poly(heptazine-triazine) Imides with Semi-coherent Interfaces for Photocatalytic Hydrogen Evolution. *Angew. Chem. Int. Ed.* **2022**, *61*, e202210849. [CrossRef]
23. Durmus, Z.; Maijenburg, A.W. A review on graphitic carbon nitride (g-C_3N_4)—Metal organic framework (MOF) heterostructured photocatalyst materials for photo(electro)chemical hydrogen evolution. *Int. J. Hydrogen Energy* **2022**, *47*, 36784–36813. [CrossRef]
24. Yu, Y.; Huang, H. Coupled adsorption and photocatalysis of g-C_3N_4 based composites: Material synthesis, mechanism, and environmental applications. *Chem. Eng. J.* **2023**, *453*, 139755. [CrossRef]
25. Llatance-Guevara, L.; Flores, N.E.; Barrionuevo, G.O.; Mullo Casillas, J.L. Waste Biomass Selective and Sustainable Photooxidation to High-Added-Value Products: A Review. *Catalysts* **2022**, *12*, 1091. [CrossRef]
26. Das, S.; Das, S.; Nair, R.G.; Chowdhury, A. Magnetically separable $ZnFe_2O_4$ grafted g-C_3N_4/rGO ternary nanocomposites for enhanced photo-Fenton catalytic activity under visible-light. *Mater. Today Sustain.* **2022**, *21*, 100263. [CrossRef]
27. Ran, J.; Jaroniec, M.; Qiao, S.Z. Cocatalysts in Semiconductor-based Photocatalytic CO_2 Reduction: Achievements, Challenges, and Opportunities. *Adv. Mater.* **2018**, *30*, 1704649. [CrossRef]
28. Lin, H.; Wu, J.; Zhou, F.; Zhao, X.; Lu, P.; Sun, G.; Song, Y.; Li, Y.; Liu, X.; Dai, H. Graphitic carbon nitride-based photocatalysts in the applications of environmental catalysis. *J. Environ. Sci.* **2023**, *124*, 570–590. [CrossRef]
29. Alaghmandfard, A.; Ghandi, K. A Comprehensive Review of Graphitic Carbon Nitride (g-C_3N_4)–Metal Oxide-Based Nanocomposites: Potential for Photocatalysis and Sensing. *Nanomaterials* **2022**, *12*, 294. [CrossRef]
30. He, Y.; Zhang, L.; Fan, M.; Wang, X.; Walbridge, M.L.; Nong, Q.; Wu, Y.; Zhao, L. Z-scheme SnO_2-x/g-C_3N_4 composite as an efficient photocatalyst for dye degradation and photocatalytic CO_2 reduction. *Sol. Energy Mater. Sol. Cells* **2015**, *137*, 175–184. [CrossRef]
31. Saraev, A.A.; Kurenkova, A.Y.; Gerasimov, E.Y.; Kozlova, E.A. Broadening the Action Spectrum of TiO_2-Based Photocatalysts to Visible Region by Substituting Platinum with Copper. *Nanomaterials* **2022**, *12*, 1584. [CrossRef]
32. Lorenz, F.; Moustakas, N.G.; Peppel, T.; Strunk, J. Comparative Studies of Oxygen-Free Semiconductors in Photocatalytic CO_2 Reduction and Alcohol Degradation. *Chem. Ing. Tech.* **2022**, *94*, 1776–1783. [CrossRef]
33. Topchiyan, P.; Vasilchenko, D.; Tkachev, S.; Sheven, D.; Eltsov, I.; Asanov, I.; Sidorenko, N.; Saraev, A.; Gerasimov, E.; Kurenkova, A.; et al. Highly Active Visible Light-Promoted Ir/g-C_3N_4 Photocatalysts for the Water Oxidation Reaction Prepared from a Halogen-Free Iridium Precursor. *ACS Appl. Mater. Interfaces* **2022**, *14*, 35600–35612. [CrossRef]
34. Dong, F.; Zhao, Z.; Xiong, T.; Ni, Z.; Zhang, W.; Sun, Y.; Ho, W.K. In situ construction of g-C_3N_4/g-C_3N 4 metal-free heterojunction for enhanced visible-light photocatalysis. *ACS Appl. Mater. Interfaces* **2013**, *5*, 11392–11401. [CrossRef]
35. Liu, H.; Chen, D.; Wang, Z.; Jing, H.; Zhang, R. Microwave-assisted molten-salt rapid synthesis of isotype triazine-/heptazine based g-C_3N_4 heterojunctions with highly enhanced photocatalytic hydrogen evolution performance. *Appl. Catal. B Environ.* **2017**, *203*, 300–313. [CrossRef]
36. Kunwar, S.; Sui, M.; Pandey, P.; Gu, Z.; Pandit, S.; Lee, J. Improved Configuration and LSPR Response of Platinum Nanoparticles via Enhanced Solid State Dewetting of In-Pt Bilayers. *Sci. Rep.* **2019**, *9*, 1329. [CrossRef]
37. Tenney, S.A.; He, W.; Ratliff, J.S.; Mullins, D.R.; Chen, D.A. Characterization of Pt-Au and Ni-Au clusters on TiO_2(110). *Top. Catal.* **2011**, *54*, 42–55. [CrossRef]
38. Steinrück, H.P.; Pesty, F.; Zhang, L.; Madey, T.E. Ultrathin films of Pt on TiO_2(110): Growth and chemisorption-induced surfactant effects. *Phys. Rev. B* **1995**, *51*, 2427–2439. [CrossRef]
39. Barr, T.L. An ESCA study of the termination of the passivation of elemental metals. *J. Phys. Chem.* **1978**, *82*, 1801–1810. [CrossRef]
40. Bernsmeier, D.; Sachse, R.; Bernicke, M.; Schmack, R.; Kettemann, F.; Polte, J.; Kraehnert, R. Outstanding hydrogen evolution performance of supported Pt nanoparticles: Incorporation of preformed colloids into mesoporous carbon films. *J. Catal.* **2019**, *369*, 181–189. [CrossRef]
41. Gołąbiewska, A.; Lisowski, W.; Jarek, M.; Nowaczyk, G.; Zielińska-Jurek, A.; Zaleska, A. Visible light photoactivity of TiO_2 loaded with monometallic (Au or Pt) and bimetallic (Au/Pt) nanoparticles. *Appl. Surf. Sci.* **2014**, *317*, 1131–1142. [CrossRef]
42. Smirnov, M.Y.; Vovk, E.I.; Nartova, A.V.; Kalinkin, A.V.; Bukhtiyarov, V.I. An XPS and STM Study of Oxidized Platinum Particles Formed by the Interaction between Pt/HOPG with NO_2. *Kinet. Catal.* **2018**, *59*, 653–662. [CrossRef]
43. Gulati, S.; Vijayan, S.; Mansi; Kumar, S.; Harikumar, B.; Trivedi, M.; Varma, R.S. Recent advances in the application of metal-organic frameworks (MOFs)-based nanocatalysts for direct conversion of carbon dioxide (CO_2) to value-added chemicals. *Coord. Chem. Rev.* **2023**, *474*, 214853. [CrossRef]

44. Domínguez-Espíndola, R.B.; Arias, D.M.; Rodríguez-González, C.; Sebastian, P.J. A critical review on advances in TiO_2-based photocatalytic systems for CO_2 reduction. *Appl. Therm. Eng.* **2022**, *216*, 119009. [CrossRef]
45. Sun, N.; Zhu, Y.; Li, M.; Zhang, J.; Qin, J.; Li, Y.; Wang, C. Thermal coupled photocatalysis over Pt/g-C_3N_4 for selectively reducing CO_2 to CH_4 via cooperation of the electronic metal-support interaction effect and the oxidation state of Pt. *Appl. Catal. B Environ.* **2021**, *298*, 120565. [CrossRef]
46. Lasia, A. Mechanism and kinetics of the hydrogen evolution reaction. *Int. J. Hydrogen Energy* **2019**, *44*, 19484–19518. [CrossRef]
47. Michaelson, H.B. The work function of the elements and its periodicity. *J. Appl. Phys.* **1977**, *48*, 4729–4733. [CrossRef]
48. Tan, L.; Xu, S.M.; Wang, Z.; Hao, X.; Li, T.; Yan, H.; Zhang, W.; Zhao, Y.; Song, Y.F. 600 nm induced nearly 99% selectivity of CH_4 from CO_2 photoreduction using defect-rich monolayer structures. *Cell Rep. Phys. Sci.* **2021**, *2*, 100322. [CrossRef]
49. Xie, S.; Wang, Y.; Zhang, Q.; Deng, W.; Wang, Y. MgO- and Pt-promoted TiO_2 as an efficient photocatalyst for the preferential reduction of carbon dioxide in the presence of water. *ACS Catal.* **2014**, *4*, 3644–3653. [CrossRef]
50. Zhai, Q.; Xie, S.; Fan, W.; Zhang, Q.; Wang, Y.; Deng, W.; Wang, Y. Photocatalytic conversion of carbon dioxide with water into methane: Platinum and Copper(I) oxide co-catalysts with a core-shell structure. *Angew. Chem.* **2013**, *52*, 5776–5779. [CrossRef]
51. Guo, Q.; Fu, L.; Yan, T.; Tian, W.; Ma, D.; Li, J.; Jiang, Y.; Wang, X. Improved photocatalytic activity of porous ZnO nanosheets by thermal deposition graphene-like g-C_3N_4 for CO_2 reduction with H_2O vapor. *Appl. Surf. Sci.* **2020**, *509*, 144773. [CrossRef]
52. Peng, H.; Guo, R.T.; Lin, H.; Liu, X.Y. Synthesis of Bi_2O_3/g-C_3N_4 for enhanced photocatalytic CO_2 reduction with a Z-scheme mechanism. *RSC Adv.* **2019**, *9*, 37162–37170. [CrossRef]